Proceedings of ASME Turbo Expo 2011
GT2011
June 6-10, 2011, Vancouver, British Columbia, Canada

GT2011-45744

EFFECTS OF ROTATION ON JET IMPINGEMENT CHANNEL HEAT TRANSFER

Justin A. Lamont and Srinath V. Ekkad
Mechanical Engineering Department
Virginia Tech
Blacksburg, VA, USA
Email: jalamont@vt.edu and sekkad@vt.edu

ABSTRACT

The effects of the Coriolis force and centrifugal buoyancy is investigated in rotating internal serpentine coolant channels in turbine blades. For complex flow in rotating channels, detailed measurements of the heat transfer over the channel surface will greatly enhance the blade designer's ability to predict hot spots so coolant air may be distributed more effectively. The present study uses a novel transient liquid crystal technique to measure heat transfer in a rotating, radially outward channel with impingement jets. This is the beginning of a comprehensive study on rotational effects on jet impingement. A simple case with a single row of constant pitch impinging jets with crossflow effect is presented to demonstrate the novel liquid crystal technique and document the baseline effects for this type of geoemtry. The present study examines the differences in heat transfer distributions due to variations in jet Rotation number and jet orifice-to-target surface distance. Colder air below room temperature is passed through a room temperature test section to simulate the centrifugal buoyancy effect seen in a real engine environment. This ensures that buoyancy is acting in a similar direction as in actual turbine blades where walls are hotter than the coolant fluid. Three parameters were controlled in the testing: jet coolant-to-wall temperature ratio, average jet Reynolds number, and average jet Rotation number. Results show, like serpentine channels, the trailing side experiences an increase in heat transfer and the leading side experiences a decrease for all jet channel height to jet diameter ratios (H/d_j). At a jet channel height to jet diameter ratio of 1, the cross-flow from upstream spent jets greatly affects impingement heat transfer behavior in the channel.

INTRODUCTION

Increasing the efficiency and output of modern gas turbines is an incremental process. A critical area of focus for increasing overall efficiency is managing the amount of coolant used. Excessive use of coolant air decreases both thermal efficiency and output of the engine, as coolant air is directly tapped from the compressor section. However, coolant air is critical in maximizing the life of the hot gas path components (turbine vanes and blades). Detailed knowledge of the heat transfer in internal coolant channels in turbine blades is required for designers to maximize cooling effectiveness while minimizing pumping power.

Coolant air is used to cool both stationary vanes and rotating blades by passing the air through intricate channels inside the airfoils to maximize heat transfer rates. Understanding coolant flow under rotation is critical because rotation adds two distinct complications: the Coriolis force and centrifugal buoyancy. The Coriolis acceleration is defined as:

$$\overrightarrow{a_c} = -2\vec{\Omega} \times \vec{V} \qquad (1)$$

where $\vec{\Omega}$ is the rotational velocity and $\vec{V}$ is the coolant velocity. The Coriolis force is dependent on the flow direction with respect to the rotational direction. The temperature difference between the channel wall and coolant flow creates buoyancy. Buoyancy coupled with centrifugal force from rotation creates a significant secondary flow. The significance of buoyant flows under rotation depends on the buoyancy parameter, which describes the free convection contribution to the overall flow pattern:

$$BP = \left(\frac{\Delta\rho}{\rho}\right)\left(\frac{R}{D_h}\right)\left(\frac{\Omega D_h}{V}\right)^2 \qquad (2)$$

where $(\Delta\rho/\rho)$ is the wall-to-coolant density ratio, (R/D_h) is the mean rotating radius-to-diameter ratio, Ω is the rotational speed, D_h is the channel hydraulic diameter, and V is the coolant velocity. The buoyancy parameter is equivalent to the ratio of the Grashof number (with $R\Omega^2$ in place of gravity) to the square of the Reynolds number, which characterizes the relative importance of free and forced convection in stationary heat transfer. Secondary flows generated by the Coriolis force and centrifugal buoyancy combine to make an asymmetric flow within the internal cooling channel. The flow pattern dictates the effectiveness of the heat transfer within the rotating blade, thus impacting the life of the component. Figure 1 (ref. 1) (left) shows the blade cross section with respect to rotational direction. The leading side of the internal coolant channel corresponds to the suction side of the blade, while the trailing side corresponds to the pressure side. Figure 1 (right) also shows a cutaway section of the blade with internal cooling channels. Typical blades have radially outward and inward flow directions.

Jet impingement cooling is already used in many industrial applications, including gas turbine heat transfer. There are numerous studies on stationary jet impingement systems. There have been studies with single jets and arrays of jets both staggered and inline. Florschuetz et al. [1] studied heat transfer distributions with a stationary array of jets with one outlet for the flow, causing spent coolant crossflow effects. Crossflow is spent coolant from upstream jets which bend downstream jets, reducing the effectiveness. Results showed that close to the outlet, the heat transfer dropped in magnitude for most arrangements due to the adverse effects of crossflow. Han et al. [2] provided a comprehensive survey of all jet impingement heat transfer papers prior to 2000. Uysal et al. [3] studied jet impingement from a single row of jets in a channel. The impingement configuration was varied with non-uniform and uniformly spaced jet holes. Results showed a decline in the heat transfer closer to the outlet. The heat transfer increased linearly with increasing Reynolds number. At high Reynolds numbers, a jet-to-jet spacing of 7.5 diameters performs slightly better than that seen in a spacing of 6.5 diameters. At lower Reynolds numbers, the difference appears to be negligible, or the 6.5 diameter spacing performs slightly better. For a jet-to-jet spacing of 6.5 diameters, a lower jet height-to-target plate distance has the highest heat transfer results.

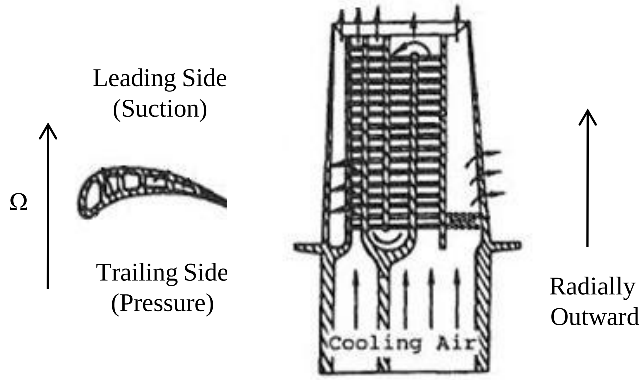

Figure 1. A standard turbine blade with internal coolant channels. (Left) cross section of blade. (right) cutaway view of coolant channels (from Parsons et al. [4]).

There have been very few published studies that have focused on rotational effects on jet impingement. One such study by Parsons et al. [4] focused on a complex rotating channel with jet impingement. Results show that under rotation, both the leading and trailing side heat transfer results are less than that seen in the stationary case. This is contrary to results seen in rib roughened channels, where heat transfer can be augmented greatly if the Coriolis force is favorable (Wagner et. al [5], Parsons et al [6], Liou and Chen [7], Taslim et. al [8]). Also, Parsons et al. [4] shows that the trailing side results are lower than that seen for the leading side. Again, for a radially outward channel with rib roughened walls, the trailing side heat transfer is favorably affected by the Coriolis force. The flow pattern generated by jet impingement is very complex, so the effect of the Coriolis force is different than for traditional rotating channels. Parsons et al. [4] uses two rows of holes; the interaction between the jets may have a greater effect on the velocity distribution, changing the effects of the Coriolis force. Parsons et al. [4] uses two rows of holes. The interaction between the jets may have a great effect on the velocity distribution, changing the effects of the Coriolis force.

The present study examines the effect of rotation on a single row of impingement holes with a crossflow exit condition similar to Uysal et al. [4]. A novel transient liquid crystal technique is used to measure local heat transfer coefficients under rotating conditions. The present study uses chilled air and room temperature walls to obtain the proper buoyancy effect for testing and to allow the use of clear acrylic walls for liquid crystal color capture. The Rotation number is a parameter which describes the ratio between rotational and inertial forces and is defined by

$$Ro = \frac{\Omega d_j}{V_j} \tag{3}$$

where Ω is the rotational speed, d_j is the diameter of the jet, and V_j is the velocity of the jet flow. The jet-to-wall temperature ratio is defined as:

$$\left(\frac{\Delta T}{T}\right) = \frac{T_w - T_j}{T_w} \tag{4}$$

where T_j is the jet temperature and T_w is the temperature of the coolant at the wall. This parameter describes the direction at which the buoyant flows operate. The jet Reynolds number was maintained around 9,000, the rotational speed was varied from 0 to 275 rpm, and the jet-to-wall temperature ratio was around 0.08.

The present study is part of a comprehensive study focusing on jet impingement cooling in rotating internal coolant channels. The present study models a single radially outward coolant channel with jet impingement. Instead of rib roughened walls, impingement jets are used to augment the heat transfer on the channel walls. A single row of constant pitch jet holes is used to demonstrate rotational effects on impingement and to validate a novel liquid crystal technique for rotating channels. Future studies will explore arrays of jets in the coolant channel. Previous rotational studies of both serpentine channels and jet impingement have highlighted the importance of the leading and trailing sides of the coolant channel, as the Coriolis force acts normally away from and into the these walls, respectively, as shown in Figure 1. Heat transfer results are presented for both leading and trailing sides under rotation.

DESCRIPTION OF TEST SETUP

The rotating channel test rig is supported by a 2m x 2m x 0.75m steel frame, as shown in Figure 2. A test section is placed on one side of the rotating arm, while a counter weight is placed on the other. A Baldor 3.73 kW (5 hp) electric motor is connected to a frequency controller which is used to set the rotational speed.

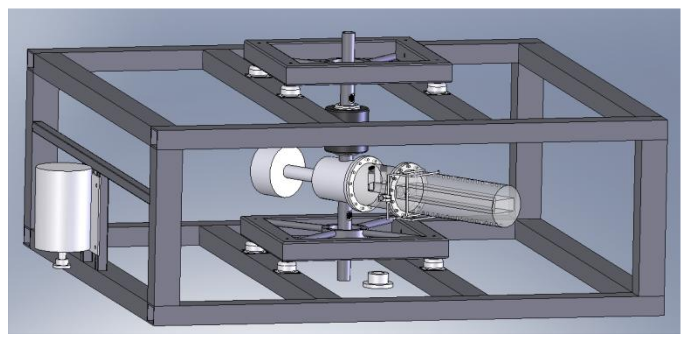

Figure 2: CAD drawing of the rotating rig support frame. The shown test section is arbitrary, as many types may be inserted.

Figure 3 shows the schematic of the rotating rig which is used to test coolant flows under rotation. A rotary union is attached to the driveshaft to allow air from the stationary source to the rotating components. A Moog slip ring allows for type k thermocouples to transmit temperature information from the rotating test section to the stationary data acquisition unit. Several 36-gage type K thermocouples are used to measure the bulk inlet and wall temperatures. The wall temperature thermocouple is taped to the wall on top of the liquid crystal coating and is used to calibrate liquid crystal color hue with temperature in an in-situ mode. Each data set collected is calibrated in-situ to prevent error due to degradation of the liquid crystals and run-to-run variations. This also improves overall uncertainty in data reductions and reduces time-lag error.

Figure 4 shows the setup to supply coolant to the test section. The setup is designed so that coolant is instantaneously injected into the test section for transient analysis. To supply the coolant (air initially at 20 °C) at the proper temperature, nitrogen gas is used to chill the coolant path to the test section. When the coolant path is suitably cooled and the test section is operating at the test rotation speed, the air direction is switched to enter the test section. Nitrogen is only used to cool down the coolant path and is not mixed with air for testing. Because of the chilling, the air temperature drops to the desired temperature and remains relatively constant for the purposes of a transient analysis. An orifice meter is used to measure the flow rate of air during the experiment.

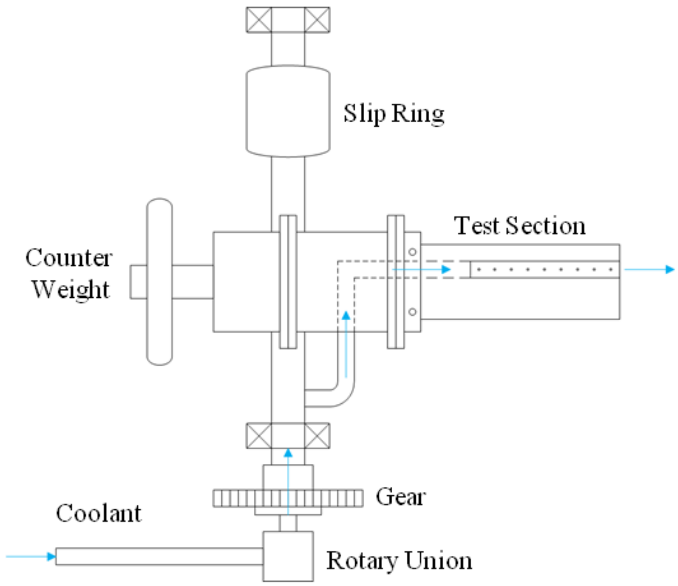

Figure 3. Schematic of the rotating rig. A camera is mounted onto the test section to view the color change in the liquid crystals.

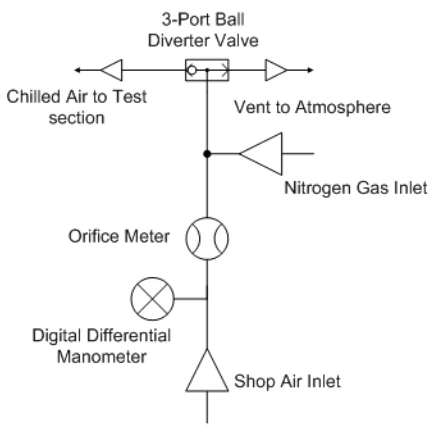

Figure 4. Schematic of the air supply to provide chilled air to the test section.

Figure 5 shows the camera mount and placement on the rotating arm. A Canon FS200 digital camcorder is mounted to the test section for filming the liquid crystal color change because of its light weight, convenient features, and onboard data storage. The camera provides images at 30 frames per second at 720 x 480 pixel resolution. Focus and white balance are fixed to prevent automatic adjustments which would introduce error when calculating the calibration curve. Calibration will be discussed in the data reduction procedure section. A mount is placed on the test section and provides a base for the camera and lighting, as shown in Figure 5. The lighting is provided by white LEDs. White light is desirable in order to clearly see the color change during a test.

Three parameters are controlled in the study: jet-to-wall temperature ratio, $\Delta T/T$; jet Reynolds number, Re_j; and jet Rotation number, Ro_j. The Reynolds number was controlled by setting the mass flow rate of air with a regulator and orifice meter. The rotation number is set by selecting a motor speed on the motor frequency controller. As shown in Figure 4, when nitrogen is vented to cool down the coolant path, the three-way diverter valve is set to vent to atmosphere. A thermocouple is placed on the valve where the nitrogen vents. It has been found that when the thermocouple at the vent reaches approximately -20°C, the coolant air temperature drops and remains at 0°C (air is initially at 20°C) during testing. All efforts are made to ensure repeatable temperatures and flow rates into the test section. A sample response of the inlet and wall temperatures is shown in Figure 6.

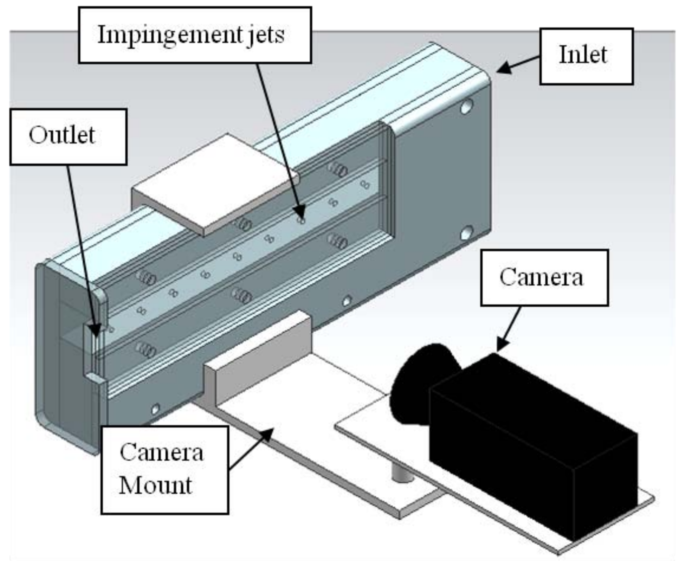

Figure 5: Illustration of test section and camera mount.

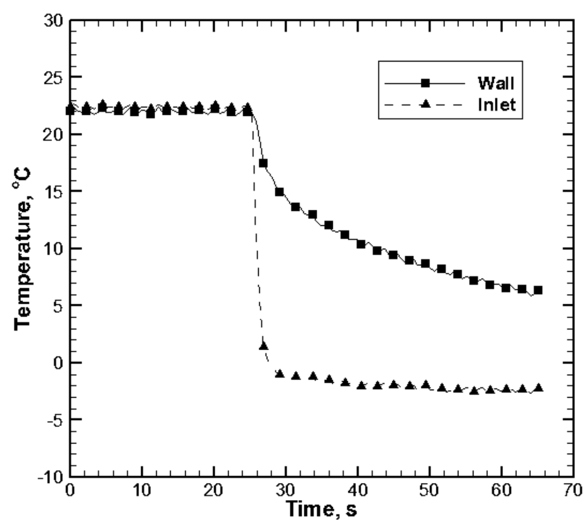

Figure 6: Temperature response for the coolant inlet and the wall temperature used for calibration.

Test Section

The test section consists of a radially outward main channel and an impingement channel. The air from the rotary union enters the rotating arms at the base of the arm into the main channel. The main channel feeds the air through the jets to the impingement channel. Figure 7 shows the square main channel with a cross section of 2.54 cm sides. The impingement channel has a width of 2.54 cm and the channel height-to-jet diameter ratio (H/d_j) can be varied By changing the side wall thickness. The overall channel length-to-jet diameter ratio (L/d_j) of the impingement channel is 72. The mean rotating radius-to-jet diameter ratio (R/d_j) of the impingement channel is 108. The jet hole diameter (d_j) was constant at 0.3175 cm (1/8th inch) for all the tests. The pitch-to-jet diameter ratio (P/d_j) of the jet holes and the jet height-to-diameter ratio (b/d_j) were also held constant at 8 and 1, respectively ([1]). The impingement channel has one outlet at the end of the channel which creates the required cross-flow effect. The liquid crystals are applied on the impingement side of the target surface. A black backing coat is applied to allow for the camera to track the color changes. To simulate leading and trailing sides, the motor rotates the test section in opposite directions, as shown in Figure 8.

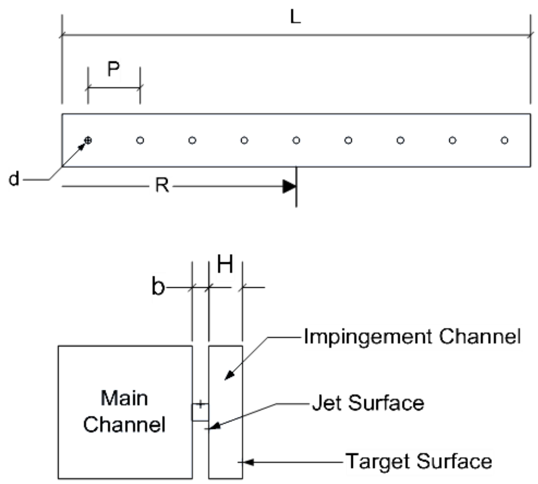

Figure 7. (Top) Lengthwise view of the test section. (Bottom) Inward view of the test section.

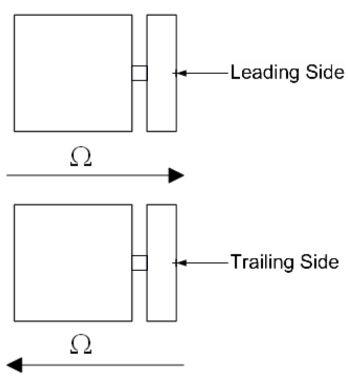

Figure 8. How the target surface changes from leading side to trailing side with different rotational direction.

DATA REDUCTION PROCEDURE

Two sources of data are taken from each experiment: video of liquid crystal color and temperature data. The video records the color change of liquid crystals, as a hue versus temperature calibration technique is used. The thermochromic liquid crystals used have a temperature range of 10-15°C (R10C5W). The temperature of the test section is initially above the color play range, so the liquid crystals start in the blue color region. The initial hue is approximately 0.5 (blue in color) across the entire surface, indicating that variations in light intensity are negligible. The light source is located next to the camera, so the maximum illumination angles are very small. A thermocouple on the wall is used to relate liquid crystal color hue with temperature by using a sample pixel area from the video next to the thermocouple. The size is arbitrary, but set large enough to capture the color change and protect against random outliers.

The starting times of the thermocouple data and the video are synchronized. As the hue around the thermocouple with respect to time is determined, it can be combined with the temperature data to develop a calibration curve. Figure 9 shows a typical calibration curve for Hue versus Temperature. A linear region is observed for a hue domain of 0.1 to 0.5. A hue of 0.1 refers to the red region and 0.5 is the blue region. The linear region is isolated and fitted with a curve. Each test run generates its own calibration curve, so Figure 9 is a typical curve for one particular test. Each test is recalibrated to prevent error from liquid crystal degradation over time or any other unforeseen occurrence. The resulting equation from the curve fit has an R^2 value no less than 0.9, indicating a strong linear correlation of the data set. The resulting equation is used to equate hue to temperature for every pixel at every frame. From the calibration curve, the time variation of temperature at each pixel is observed. Each pixel has a unique change in temperature, therefore a unique heat transfer coefficient.

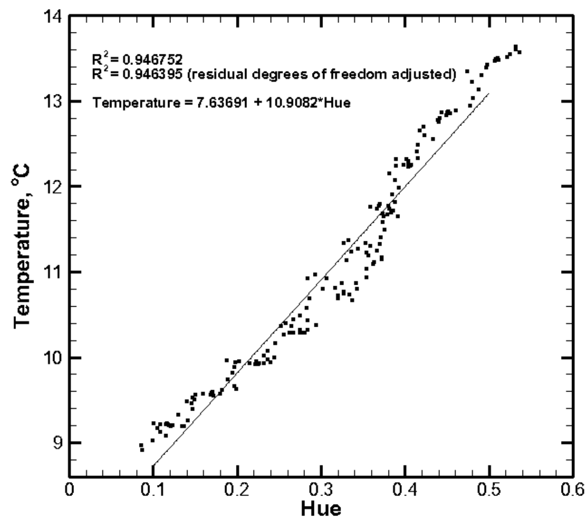

Figure 9: Calibration curve relating hue to temperature. The relationship is approximately linear.

The test section and test conditions were designed to model a semi-infinite solid with convection at the surface under transient conditions. This assumption is valid as long as the thermal penetration due to conduction does not extend all the way through the material (causing 2-D conduction effects). Because the thermal diffusivity of acrylic is very low, the maximum allowable testing time is approximately 80 seconds for a 3.175 mm thick plate. The typical testing time is approximately 20-30 seconds, well below the maximum. Therefore, the semi-infinite solid assumption is valid (1-D conduction). With the semi-infinite solid assumption, the following mathematical function is valid (Incropera et al. [9]):

$$\frac{T(0,t)-T_i}{T_\infty - T_i} = 1-\left[\exp\left(\frac{h^2\alpha t}{k^2}\right)\right]\left[erfc\left(\frac{h\sqrt{\alpha t}}{k}\right)\right] \qquad (5)$$

where T_i is the initial wall temperature, T_∞ is the bulk temperature, α is the thermal diffusivity of the acrylic, t is the time, h is the heat transfer coefficient, and k is the thermal conductivity of the acrylic. Properties were determined based on the film temperature. Bulk temperature and initial wall temperature are measured with thermocouples. T(0,t) is the wall temperature at a given pixel location for every frame determined by applying the calibration curve. Figure 6 shows a typical wall temperature history of a single pixel. This is the simplified equation because the wall surface where the liquid crystals are applied corresponds to x=0. The only unknown is h. Although only one wall temperature and time data pair is needed to solve the equation for the heat transfer coefficient, to reduce errors, data is collected over the range of the liquid crystal range and test duration. Since the liquid crystal paint chosen was able to give wall temperatures over a wide range of temperatures, a regression analysis method was used to eliminate random errors in recorded local wall temperatures which range up to 30 seconds of data at 30 frames/second. The regression analysis put all terms of the conduction equation to the right hand side of the equation and was solved for all points of data for each pixel. This resulted in a residual error for each time-temperature data pair. The residual error was minimized in a least squares sense solving for the heat transfer coefficient that best fit all data. This reduced the random camera read errors (due to lighting variations) of the liquid crystal paint and also relaxes the dependence on the initial temperature of the target plate on the results. Once h is determined, the Nusselt number is calculated by

$$Nu = \frac{hd_j}{k} \tag{6}$$

where h is the local heat transfer coefficient, d_j is the jet diameter, and k is the local thermal conductivity of the air.

Uncertainty

Uncertainty in the heat transfer coefficient, h, is determined by evaluating the individual uncertainties in the measurements. The measurement uncertainty in the initial, mainstream, and wall temperature (T_i, T_∞, and T_w, respectively) are all 0.6 °C. The uncertainty in the time step of the camera is approximately 16ms. There is a 6% measurement uncertainty in the material properties. Overall, with the hue vs. temperature calibration technique, the overall uncertainty is approximately ±7%. Uncertainties and techniques are similar to that of Esposito et al [10]. The calibration and technique for the liquid crystals is explained in detail in Ekkad and Han [11] and Camci et al [12]. The method of Kline and McClintock [13] was used to assess overall uncertainty.

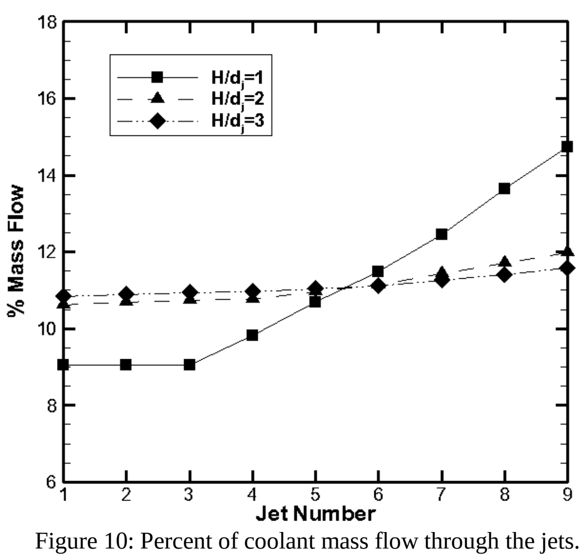

Figure 10: Percent of coolant mass flow through the jets.

RESULTS AND DISCUSSION

Results presented in this section show how rotation affects heat transfer on the leading and trailing side walls compared to a stationary wall. The flow distribution is calculated for the stationary cases to verify that the model is consistent with expectations and previous studies. It is used to help explain the heat transfer results as well. Results are presented by determining the area average heat transfer (also referred to as the mean value) for each jet and the maximum value for each jet. The impingement channel size was varied by altering the distance from the jet surface to the target surface (H) by H/d_j=1,2, and 3. Results are presented by exploring how rotation affects the individual H/d_j cases. The H/d_j results are then directly compared to each other. Heat transfer analysis includes the first seven jets, whereas the flow distribution is calculated for all nice. The buoyancy parameter for all cases is much less than 1, meaning for these particular experiments, buoyancy was not a dominating factor for the flow patterns. Each case ran at Re_j=9,000; $\Delta T/T$ = 0.08; and varied from Ro_j=0 to 0.0022.

Flow Distribution

Unlike the setup of Uysal et al. [3] where the inlet flow is normal to the impingement jet faces, the inlet flow of the present study runs parallel to the impingement jet faces. With pressure measurements of the stationary case, the flow through each jet is determined to not be evenly distributed. This is evident in Figure 10, as the percent mass flow of coolant through each jet rises from jet 1 to jet 7. Mass flow through each jet was determined using the same method discussed in Gritsch etl a. [14] The rise is more subtle in H/d_j=2 and 3. A substantial rise occurs in H/d_j=1. Figure 11 shows the ratio of the mass flux of coolant crossflow to the mass flux through the individual jets (G_c/G_j). All the three cases show similar trends with crossflow becoming stronger for downstream jets. The G_c/G_j ratio for H/d_j=1 rises more quickly and reaches the highest overall level, indicating stronger crossflow. The small cross sectional area of the H/d_j=1 impingement channel leads to a high mass flux of crossflow. The high mass flux through the impingement channel leads to lower pressures, which results in the higher coolant flow rate for downstream jets, explaining why the downstream jets for the H/d_j=1 case show a higher percentage of the total coolant mass flow.

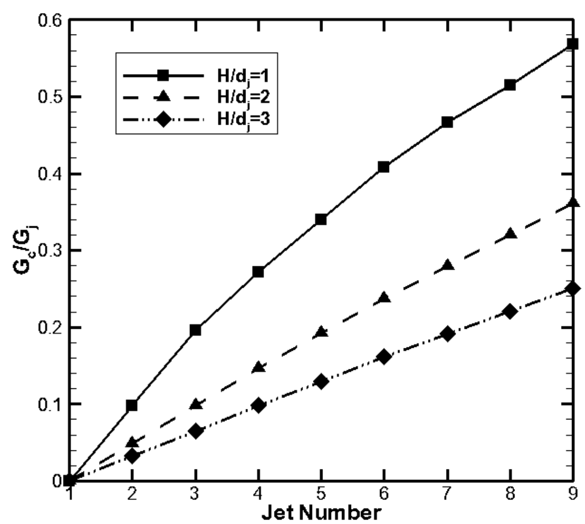

Figure 11: Ratio of crossflow-to-jet mass flux for the jets.

Rotational effects on H/d_j=1

Figure 12 shows the detailed results for the heat transfer on the target surface. From a qualitative standpoint, the trailing side heat transfer is consistently higher than the leading side and stationary results. This is expected, as stated earlier, due to the previous studies on serpentine channels by Wagner et al. [5], Parsons et al. [6], Liou and Chen [7], and Taslim et al. [8] However, this is in disagreement with Parsons et al. [4]. Parsons et al. [4] had impingement channels on both sides at the same time, whereas the present study uses one single impingement channel. Parsons et al. [4] also used two rows of impingement jets at a similar Re, so more mass flow was going through the impingement channel and different heat transfer

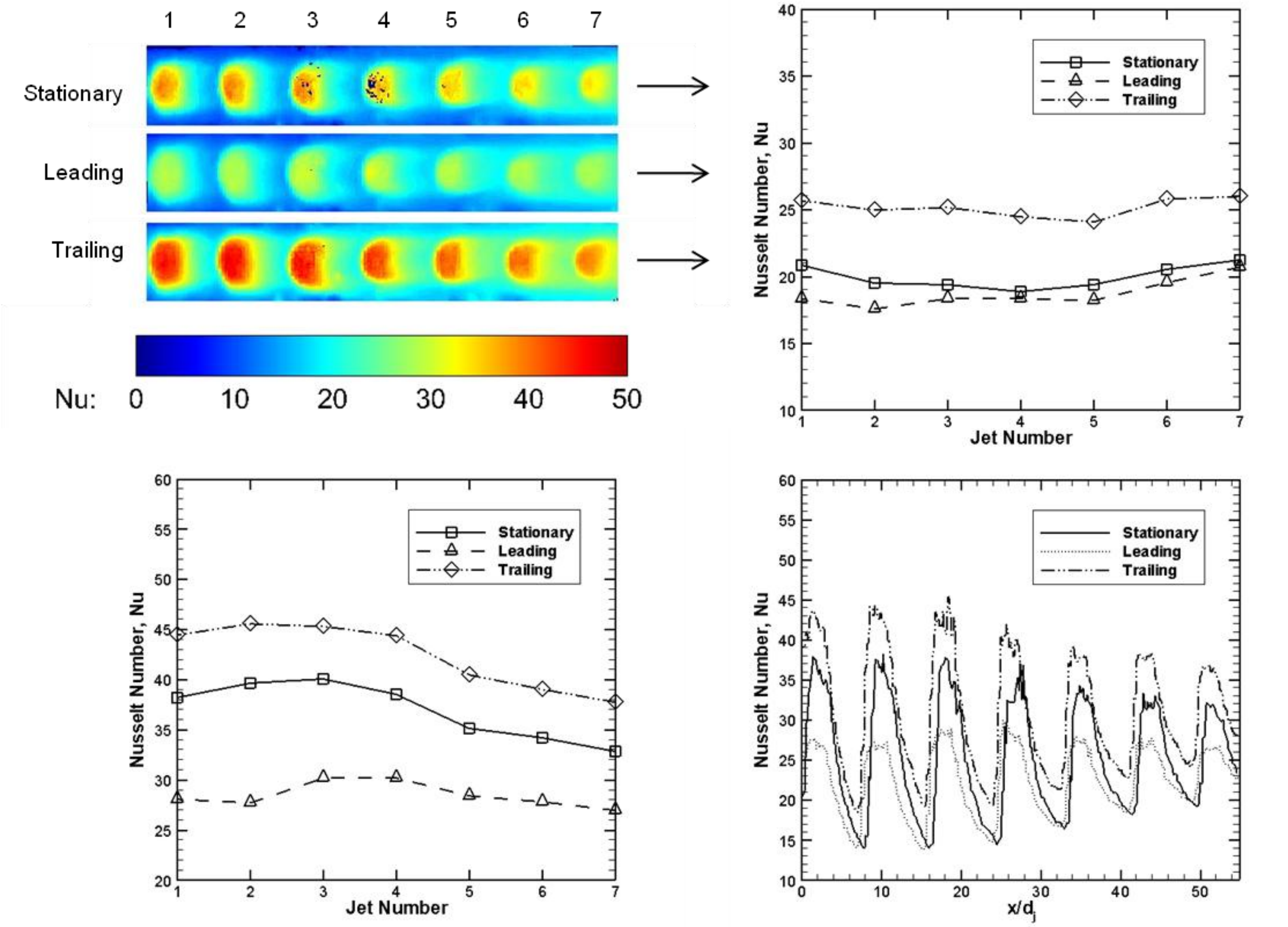

Figure 12: H/d_j=1. (Top left) Detailed results: (Top right) Area average jet heat transfer. (Bottom left) Maximum jet heat transfer. (Bottom right) Midline rake of the heat transfer along the channel length.

behavior. Figure 12 shows the mean and maximum values of heat transfer. The mean value rises from jet 1 to jet 7, while the maximum values decrease. Crossflow from previous jets act to bend the later jets away from the target surface. This explains why there is a decrease in the maximum values. The detailed results show that by jet 3, the heat transfer distribution under the jet appears to be a crescent instead of circular. This is a sign of the crossflow bending the jets. However, towards the end of the channel, there is more mass flow of coolant through the impingement channel. With more mass flow, the coolant velocity increases. The velocity increase appears to be significant enough to increase the overall heat transfer in the channel. This greatly helps the leading side, because it counteracts the detrimental effects of the Coriolis force. The Coriolis forceincreases the slope of the boundary layer on the trailing side, increasing heat transfer. The leading side experiences a decrease in the slope of the boundary layer, reducing heat transfer. The counteraction of the crossflow is apparent in the midline rake plot of the channel. The minimum values are increasing, while the maximum values are decreasing. This shows that the crossflow is becoming more influential on the jets, in terms of heat transfer on the target surface. From Table 1a, the leading side has the largest mean gain in heat transfer from jet 1 to jet 7. This is due to the crossflow, which counteracts the detrimental effects of the Coriolis force. The trailing side only sees slight gains, because the Coriolis force is already augmenting the heat transfer. Table 1b shows the average percent change in heat transfer between the trailing side and leading side with the stationary case. The trailing side sees the largest gains due to the combination of crossflow and the Coriolis force augmenting heat transfer. The Coriolis force affects the main channel, causing the trailing side to be the high pressure side and the leading side to be the low pressure side. The high pressure of the trailing side forces the coolant through the jets faster causing the heat transfer on the trailing side to be higher than the leading side.

Table 1a. H/d_j=1. Percent difference in mean and max heat transfer values between jet 1 and jet 7.

	Mean	Max
Stationary	1.9	-14.0
Leading	12.6	-3.7
Trailing	1.3	-15.0

Table 1b. H/d_j=1. Average percent difference between rotational cases and the stationary case.

	Mean	Max
Leading	-6.2	-22.6
Trailing	26.1	14.9

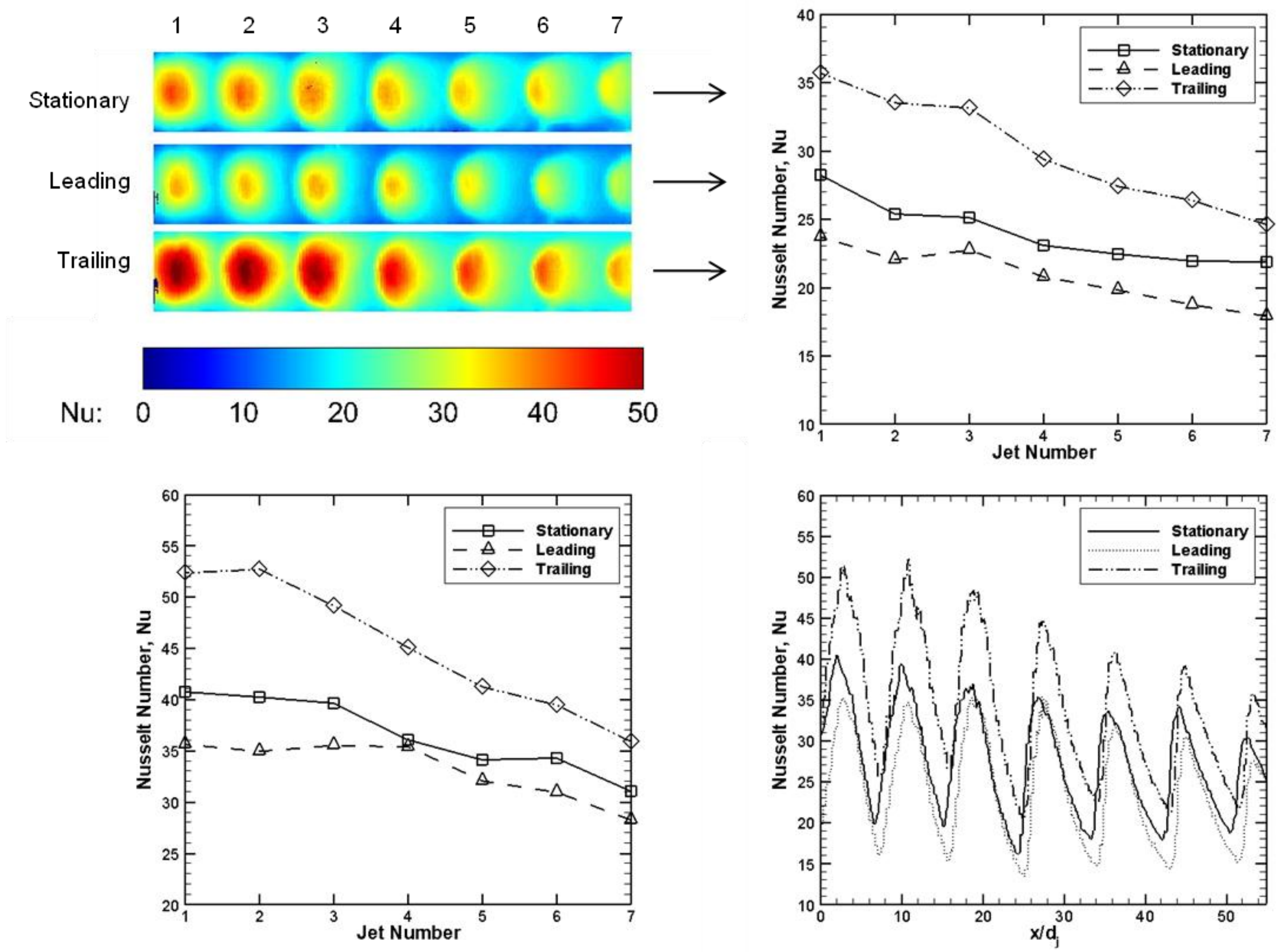

Figure 13: H/d_j=2. (Top left) Detailed results: (Top right) Area average jet heat transfer. (Bottom left) Maximum jet heat transfer. (Bottom right) Midline rake of the heat transfer along the channel length.

Rotational effects on H/d_j=2

Figure 13 shows the detailed results for the heat transfer on the target surface. Similar to the H/d_j=1 results, the trailing side heat transfer appears to be higher than the leading side and stationary results. The heat transfer on the trailing side clearly has higher maximum values at the center of the jets compared to the leading side and stationary cases. Also, in the area between the jets, the heat transfer is highest for the trailing side. Figure 13 shows that both the mean and maximum heat transfer values drop across the channel. The channel is twice as large compared to the H/d_j=1 case, so the crossflow velocity is only half. This would cause a reduction in heat transfer due to the crossflow itself and decrease its influence on the jets. The crossflow effect is still present, as the heat transfer distribution under the jets become crescent shaped around jet 5. The effect is not as pronounced as in H/d_j=1, as shown in the midline rake. The minimum values appear to remain constant, not rising. It still has an effect on the maximum values, as they drop from jet 1 to jet 7. Table 2a shows the percent drop from jet 1 to jet 7. The trailing side shows the largest drop in heat transfer. This could be due to the Coriolis force. Although it has beneficial effects for the developing crossflow, as seen in H/d_j=1, it has detrimental effects on the jets. The developing boundary layer protects the target surface from the incoming jet, reducing the effectiveness of the jets. The leading side experiences a large increase in the boundary layer on the jet surface, where the coolant jets have the highest velocity. The high velocity of the jet opening allows the jets to resist the crossflow better than at the target surface. Table 2b shows the percent change in heat transfer between the leading side and trailing side compared to the stationary case. The Coriolis force affects the main channel, causing the trailing side to be the high pressure side and the leading side to be the low pressure side. The high pressure of the trailing side forces the coolant through the jets faster causing the heat transfer on the trailing side to be higher than the leading side.

Table 2a. H/d_j=2. Percent difference in mean and max heat transfer values between Jet 7 and Jet 1.

	Mean	Max
Stationary	-22.5	-23.7
Leading	-24.4	-20.8
Trailing	-31.0	-31.4

Table 2b. H/d_j=2. Average percent difference between rotational cases and the stationary case.

	Mean	Max
Leading	-13.26	-8.91
Trailing	24.66	22.85

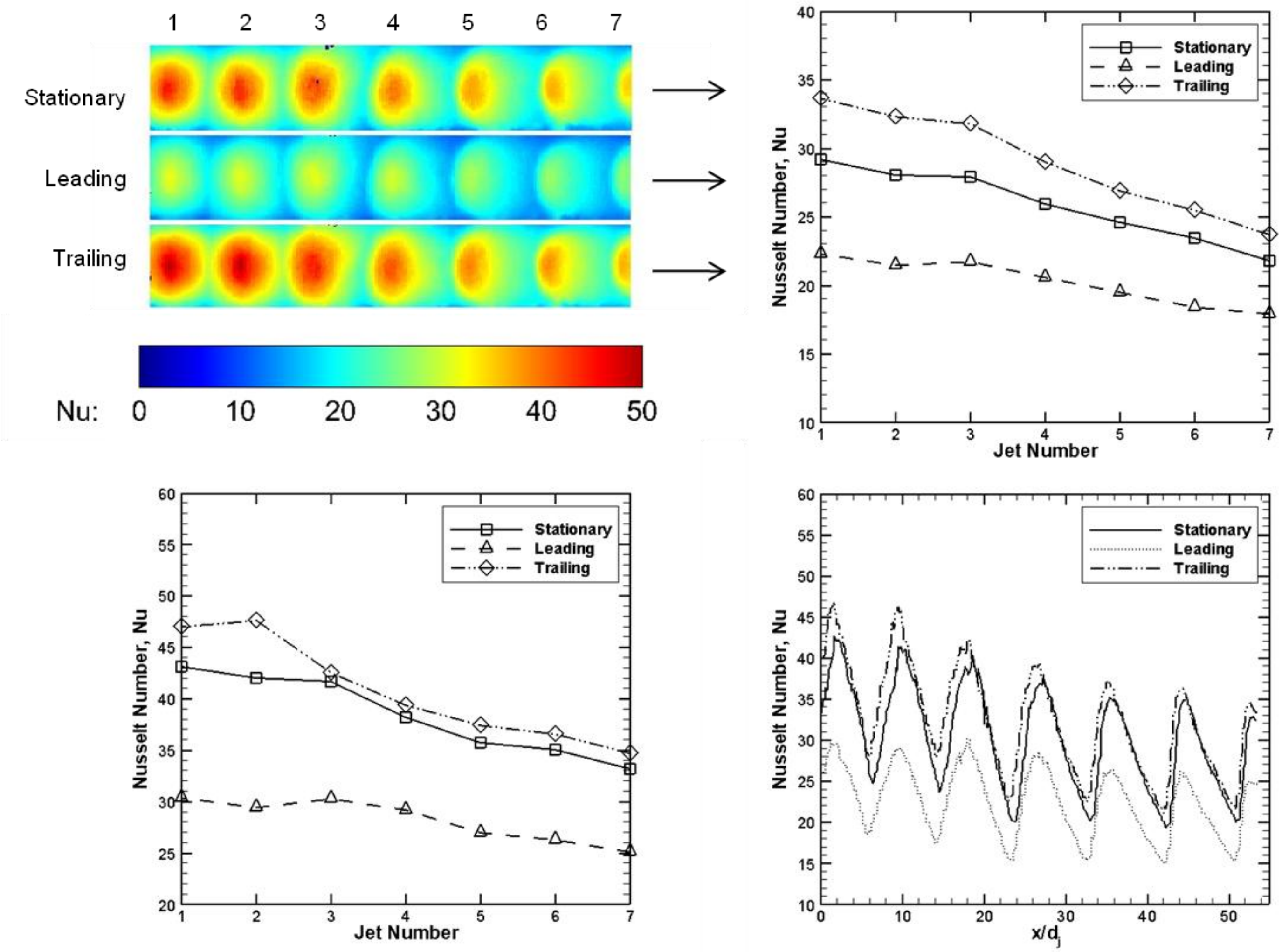

Figure 14: H/d_j=3. (Top left) Detailed results: (Top right) Area average jet heat transfer. (Bottom left) Maximum jet heat transfer. (Bottom right) Midline rake of the heat transfer along the channel length

Rotational effects on H/d_j=3

Much like the H/d_j=2 case, the trailing side experiences an overall increase in heat transfer over the stationary case, while the leading side experiences an overall decrease in heat transfer. Figure 14 shows the mean and maximum heat transfer values drop across the channel. This is similar to the H/d_j=2 case, in that the crossflow does not increase the heat transfer in the channel, but acts to only bend the jets away from the target surface, decreasing overall heat transfer. The midline rake plot shows that the minimum values are actually dropping, demonstrating the ineffectiveness of the crossflow to aid in heat transfer. The crossflow velocity is about $1/3^{rd}$ that of the H/d_j=1 case, but still causes an impact because of the large area it acts over The crossflow effect is evident in the detailed plots by about jet 6, where the heat transfer distribution begins to crescent. Comparing H/d_j=2 to 3, there is less crossflow mass flux to bend the jets away from the target surface for case 3. This is why there is less percent change from jet 1 to jet 7 for case 3 than case 2.

Table 3a. H/d_j=3. Percent difference in mean and max heat transfer values between jet 7 and Jet 1.

	Mean	Max
Stationary	-25.20	-22.96
Leading	-19.92	-17.17
Trailing	-29.58	-26.08

Table 3b. H/d_j=3. Average percent difference between rotational cases and the stationary case.

	Mean	Max
Leading	-20.87	-26.09
Trailing	12.52	6.20

Comparisons between H/d_j cases

Stationary. Figure 15a shows the mean heat transfer in the impingement channel as H/d_j is varied from 1 to 3. As H/d_j is increased, so does the heat transfer values for all jets. For the first jet, crossflow is not present. In comparison to single jet studies, as H/d_j increases, the heat transfer increases until a certain threshold is reached. According to Gardon and Carbonpue [15], an H/d_j=6 is the threshold. In Figure 15a, a large increase in heat transfer is seen from H/d_j=1 to 2, and a small change from H/d_j=2 to 3. By examining Figure 10, the percent mass flow through the first jet is considerably less for the H/d_j=1 case. There is only a slight difference in percent mass flow through the first jet from H/d_j=2 to 3. For the remaining jets, the effect of the crossflow is evident. For H/d_j=2 and 3, the mean heat transfer has a steady decline from jet 1 to jet 7. The mass flux of crossflow acts to bend the jets away from the target wall. For H/d_j=1, the crossflow is very significant. From Figure 11, the ratio of crossflow-to-jet mass flux is considerably larger than the other two cases. The mass flux is significant enough that the heat transfer begins to increase towards the end of the channel.

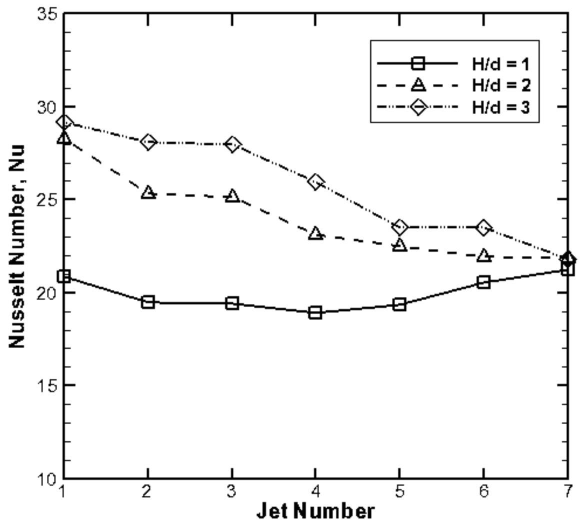

Figure 15a. H/d_j comparison for the stationary case.

Leading Side. Figure 15b shows the mean heat transfer in the impingement channel as H/d_j is varied from 1 to 3. As discussed earlier, all H/d_j results are lower than their corresponding stationary results. Distributions are similar, H/d_j=1 shows an increase at the end of the channel, while H/d_j=2 and 3 show a steady decline. A major difference is that the H/d_j=3 case is lower than H/d_j=2. Several factors may account for this. The first jet does not experience crossflow, however, the H/d_j=2 is greater than H/d_j=3. The Coriolis force may affect the main channel feeding the impingement jets. The distribution of mass flow through the jets would be affected. The amount of mass flow through jet 1 must be reduced, altering the local jet Reynolds number causing a reduction in heat transfer. The larger channel of H/d_j=3 produces a lower mass flux of crossflow. Due to the lower amount of mass flux, the Coriolis force plays a more dominating role in deflecting the jets away from the target surface.

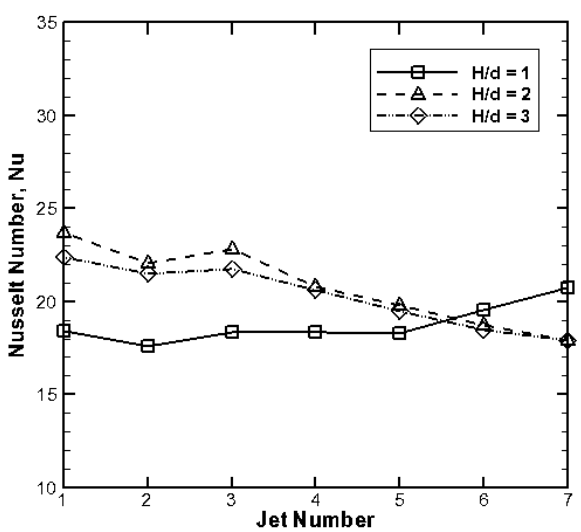

Figure 15b. H/d_j comparison for the leading side case.

Trailing Side. Figure 15c shows the mean heat transfer in the impingement channel as H/d_j is varied from 1 to 3. As discussed earlier, all H/d_j results are higher than their corresponding stationary results. The H/d_j=1 case shows the strong effects of crossflow as the end of the channel experiences a rise in heat transfer. Similar to the leading side, the H/d_j=2 case is slightly higher than H/d_j=3. This may be due to the change in mass flow distribution among the jets. Less mass flow may be going through the beginning jets, reducing the heat transfer. Similar to the leading side, the Coriolis force may play a more dominant role as the crossflow mass flux for H/d_j=3 is lower than that of the other two cases.

General trends have been validated. To validate the magnitudes of the results, single jet impingement studies are used for comparison. This is valid for jet 1 in the present study's channel, because there is little to not crossflow at that point. Huang and Mohammed [16] studied the effect of Reynolds number and jet-to-plate distance on heat transfer. For a Re_j=6000 case, heat transfer results indicate maximum Nusselt numbers at the center of the jet are slightly below 40 for H/d=1 and slightly above 40 for H/d=2. This is close to the present study's maximum values for the stationary case, with similar Re.

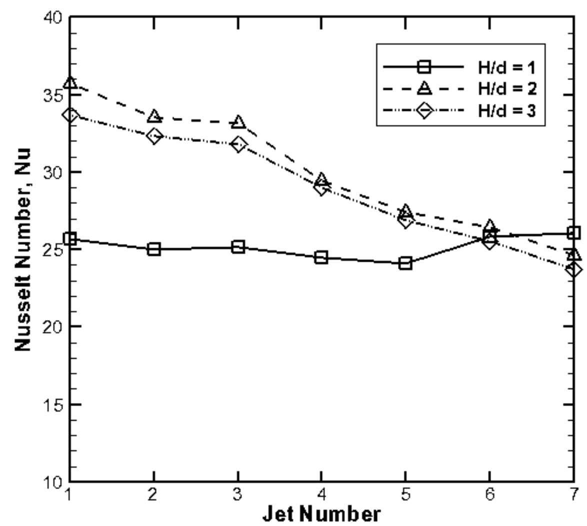

Figure 15c. H/d_j comparison for the trailing side case.

CONCLUSIONS

Detailed heat transfer distributions were measured using a novel transient liquid crystal technique for a rotating impingement channel. A camera was mounted on a rotating test section to film the liquid crystal's color change. This is the first demonstration of a liquid crystal technique to obtain detailed heat transfer distributions under rotating conditions matching the required buoyancy direction as seen in gas turbine blades. The results are the beginning of a comprehensive study on detailed measurements of rotating blade heat transfer for gas turbines. The study of a simple rotating coolant channel with single row of impingement holes is used to demonstrate the quality of the measurements using this technique and will also help gain significant insight into the potential of using jet impingement as the dominant mode of convective cooling in rotating blades.

Results indicate that under the prescribed flow conditions in the experiments, there is an ideal H/d_j for rotating channels which is different from an ideal H/d_j for stationary channels. An H/d_j of 3 is clearly the best (of the three cases studied) for the stationary case which is consistent with numerous studies on stationary impingement, while the rotating cases appear to be best at an H/d_j of 2. Results clearly show similarities when compared to 2-pass coolant channels with rib roughened walls. For radially outward flow, the trailing side experiences the Coriolis force favorably. This increases the heat transfer on that wall. The leading side experiences a detrimental effect from the Coriolis force. The same phenomenon is affecting jet impingement in the present configuration but with the the additional complexity of crossflow and jet length. Future studies will explore velocity measurements on a rotating frame, multi row jet arrays, different jet-to-jet pitch lengths, and varying impingement angles.

NOMENCLATURE

a_c	Coriolis Acceleration = $-2\Omega \times V$
V	Mainstream Velocity
(R/D_h)	Mean Rotating Radius to Hydraulic Diameter Ratio
R	Mean Rotating Radius
d_j	Jet Diameter
D_h	Hydraulic Diameter of Impingement Channel=4A/P
A	Cross Sectional Area
P	Perimeter of the Channel
L	Channel Length
BP	Buoyancy Parameter = $(\Delta\rho/\rho)(R/D_h)(\Omega D_h/V)^2$
Ro_j	Jet Rotation Number = $\Omega d_j/V$
Re_j	Jet Reynolds Number = Vd_j/υ
$\Delta T/T$	Coolant-to-wall temperature ratio= $(T_w-T_j)/T_w$
T_w	Wall Temperature
T_j	Jet Temperature
(L/d_j)	Passage Length to Hydraulic Diameter Ratio
T(0,t)	Wall Temperature at Surface
T_i	Initial Wall Temperature
T_∞	Mainstream Temperature
h	Heat Transfer Coefficient
t	Time
k	Thermal Conductivity
Nu	Nusselt Number = hd_j/k
Pr	Prandtl Number
G_c	Mass Flux of Coolant Crossflow
G_j	Mass Flux through Jet
Greek Symbols	
α	Thermal Diffusivity of Acrylic Target Plate
$(\Delta\rho/\rho)_i$	Inlet Density Ratio = $(\rho_b - \rho_w)/\rho_b$
ρ_b	Bulk Coolant Density
ρ_w	Coolant Density at Wall Temperature
υ	Kinematic Viscosity of Coolant

ACKNOWLEDGMENTS

The authors would like to thank DOE-NETL for funding part of the work under the Regional University Alliance (RUA) through URS corporation. Program monitors are Dr. Mary Anne Alvin from NETL and Dr. Vijay Jain from URS. The primary author would also like to thank the NSF GANN fellowship provided through the Virginia Tech Mechanical Engineering Department.

REFERENCES

[1] Florschuetz, L.W., Truman, C.R., and Metzger, D.E., 1981. "Streamwise Flow and Heat Transfer Distributions for Jet Array Impingement with Crossflow". Journal of Heat and Mass Transfer, **103**, pp. 337-342.

[2] Han, J.C., Dutta, S., and Ekkad, S.V., 2000, *Gas Turbine Heat Transfer and Cooling Technology*, Taylor and Francis, Inc.

[3] Uysal, U., Li, P.-W., Chyu, M.K., and Cunha, F.J., 2005. "Heat Transfer on Internal Surfaces of a Duct Subjected to Impingement of a Jet Array with Varying Jet Hole-Size and Spacing". Journal of Turbomachinery, **128**, pp. 158-165.

[4] Parsons, J.A., Han, J.C., and Lee, C.P., 1998. "Rotation Effect on Jet Impingement Heat Transfer in Smooth Rectangular Channels with Four Heated Walls and Radially Outward Crossflow". Journal of Turbomachinery, **120**, pp. 79-85.

[5] Wagner, J.H., Johnson, B.V., and Kopper, F.C., 1991. "Heat Transfer in Rotating Serpentine Passages with Smooth Walls". Journal of Turbomachinery, **113**, pp. 321-330.

[6] Parsons, J.A., Han, J.C., and Zhang, Y., 1994. "Wall Heating Effect on Local Heat Transfer in a Rotating Two-Pass Square Channel with 90° Rib Turbulators". International Journal of Heat and Mass Transfer, **37**, pp. 1411-1420.

[7] Liou, T.M., Chen, C.C., and Chen, M.Y., 2001. "TLCT and LDV Measurements of Heat Transfer and Fluid Flow in a Rotating Sharp Turning Duct". International Journal of Heat and Mass Transfer, **44**, pp. 1777-1787.

[8] Taslim, M.E., Rahman, A., and Spring, S.D., 1991. "An Experimental Investigation of Heat Transfer Coefficients in a Spanwise Rotating Channel with Two Opposite Rib-Roughened Walls". Journal of Turbomachinery**, 113**, pp. 75-82.

[9] Incropera, F.P., DeWitt, D.P., Bergman, T.L., and Lavine, A.S., 2007. *Fundamentals of Heat and Mass Transfer 6th Edition.* John Wiley and Sons. Hoboken, NJ. pp 283-290.Chap. 5.

[10] Esposito, E.I., Ekkad, S.V., Kim, Y., and Dutta, P., 2009. "Novel Jet Impingement Cooling Geometry for Combustor Liner Backside Cooling." Journal of Thermal Science and Engineering Applications, **1**, pp 021001-1 – 021001-8.

[11] Ekkad, S.V., and Han, J.C., 2000. "A Transient Liquid Crystal Thermopgraphy Technique for Gas Turbine Heat Transfer Measurements." Measurement Science and Technology, **11**, pp 1-12.

[12] Camci, C., Kim, K., and Hippensteele, S.A., 1992. "A New Hue Capturing Technique for the Quantitative Interpretation of Liquid Crystal Images Used in Convective Heat Transfer Studies." Journal of Turbomachinery, **114**, pp 765-775.

[13] Kline, S.J., and McClintock, F.A., 1953. "Describing Uncertainties in Single Sample Experiments." Mech Eng. (Am. Soc. Mech. Eng.), **75**, pp 3-8.

[14] Gritsch, M., Schulz, A., and Wittig, A., 1998. "Discharge Coefficient Measurements of Film-Cooling Holes with Expanded Exits." Journal of Turbomachinery, **120**, pp 557-563.

[15] Gardon, R. and Carbonpue, J., 1962. "Heat Transfer between a flat plate and jets of air impinging on it". Int. Developments in Heat Transfer, Int. Heat Transfer Conf., University of Colorado, CO, USA, August 28 to September 1, **2**, 454-460.

[16] Huang, L. and Mohamed, S.E., 1994. "Heat Transfer of an Impinging Jet on a Flat Surface". International Journal of Heat and Mass Transfer, **37**, pp 1915-1923.

[17] Hsieh, S.-S., Huang, J.-T., and Liu, C.-F., 1999. "Local Heat Transfer in a Rotating Square Channel with Jet Impingement". Journal of Heat Transfer, **121**, pp. 811-818.

[18] Cho, H.H. and Rhee, D.H., 2001. "Local Heat/Mass Transfer Measurement on the Effusion Plate in Impingement/Effusion Cooling Systems". Journal of Turbomachinery, **123**, pp. 601-608.